
Subject Section

Marker Controlled Superpixel Nuclei Segmentation and Automatic Counting on Immunohistochemistry Staining Images

Jie Shu^{1, 2,*}, Jingxin Liu³, Yongmei Zhang¹, Hao Fu⁴, Mohammad Ilyas⁵, Giuseppe Faraci⁶, Vincenzo Della Mea⁶, Bozhi Liu³ and Guoping Qiu^{3, 7}

¹School of Information Science and Technology, North China University of Technology, Beijing, 100144, China and

²Beijing Key Laboratory on Integration and Analysis of Large-scale Stream Data, Beijing, 100144, China and

³Shenzhen University & Guangdong Key Laboratory for Intelligent Signal Processing, Guangzhou, 518061, China and

⁴College of Intelligence Science and Technology, National University of Defense Technology, Hunan, 410073, China and

⁵Faculty of Medicine & Health Sciences, Nottingham University Hospitals NHS Trust and University of Nottingham, Nottingham, NG7 2UH, UK and

⁶Department of Mathematics, Computer Science and Physics, University of Udine, Udine, 33100, Italy and

⁷Department of Computer Science, University of Nottingham, Nottingham, NG8 1BB, UK.

*To whom correspondence should be addressed.

Associate Editor: XXXXXXX

Received on XXXXX; revised on XXXXX; accepted on XXXXX

Abstract

Motivation: For the diagnosis of cancer, manually counting nuclei on massive histopathological images is tedious and the counting results might vary due to the subjective nature of the operation.

Results: This paper presents a new segmentation and counting method for nuclei, which can automatically provide nucleus counting results. This method segments nuclei with detected nuclei seed markers through a modified simple one-pass superpixel segmentation method. Rather than using a single pixel as a seed, we created a superseed for each nucleus to involve more information for improved segmentation results. Nucleus pixels are extracted by a newly proposed fusing method to reduce stain variations and preserve nucleus contour information. By evaluating segmentation results, the proposed method was compared to five existing methods on a dataset with 52 immunohistochemically (IHC) stained images. Our proposed method produced the highest mean F1-score of 0.668. By evaluating the counting results, another dataset with more than 30,000 IHC stained nuclei in 88 images were prepared. The correlation between automatically generated nucleus counting results and manual nucleus counting results was up to $R^2 = 0.901$ ($p < 0.001$). By evaluating segmentation results of proposed method-based tool, we tested on a 2018 Data Science Bowl (DSB) competition dataset, three users obtained DSB score of 0.331 ± 0.006 .

Availability: The proposed method has been implemented as a plugin tool in ImageJ and the source code can be freely downloaded.

Contact: shujie@ncut.edu.cn

Supplementary information: Supplementary data are available at <https://www.dropbox.com/sh/e7oz4nhp3gekvk4/AAC-xuqg5DUx0H5JdqPApbWTa?dl=0> online.

1 Introduction

Immunohistochemistry (IHC) is a technique that has been widely used in cancer diagnosis. It locates and stains target biomarkers

with a specific colour (positive) against another colour (negative) counterstain. Pathologists examine the distribution of stained biomarkers to make clinical decisions. For nuclear activity-based histopathological assessments, such as the protein ki67-index Barricelli *et al.* (2019), Nottingham prognostic index plus Liu *et al.* (2018), and the others Braun *et al.* (2013); Wang *et al.* (2015); Sirinukunwattana *et al.* (2016); Irshad *et al.* (2014), one of the most important pieces of information is the number of nuclei, which requires the accurate segmentation of positively stained cell nuclei. Manual nucleus counting is time consuming and prone to intra- and inter-observer discrepancies. Therefore, an automatic, robust and accurate nucleus counting method is very important for making objective and reproducible clinical decisions. However, uneven staining and clustered or overlapping nuclei may complicate segmenting and counting nuclei in IHC stained images.

The detection of nuclei through intensity thresholding method is efficient, and was largely used in a previous paper Phoulady *et al.* (2016), but might not compensate for the issue of uneven staining. Although biomarkers normally accumulate in the nucleus, the detection of staining for a specific biomarker Casiraghi *et al.* (2017, 2018) may not work for extracting nucleus pixels for a number of background pixels also stained the same colour. To compensate for uneven staining, Huang and Lai (2010); Veta *et al.* (2011) performed dual-morphological transformation before thresholding. However, since intensity changes across the whole image, global thresholding may miss nuclei with weak intensity values and falsely identify pixels adjacent to nuclei boundaries as nucleus pixels. By focusing on blob-like shapes Al-Kofahi *et al.* (2010), it has the potential to compensate for uneven staining, but might lead to other problems, i.e. missing shape characteristics.

To split nuclei with clustering and overlapping issues, several contour characteristics have been computed to determine splitting lines, i.e. contour curvature Zafari *et al.* (2015); Al-Kofahi *et al.* (2010); Phoulady *et al.* (2016) and contour concave points Zhang and Li (2017). However, the contour of nuclei in severely clustered and overlapping regions might be missing, so it is impossible to compute these characteristics; moreover, the computation cost may be as high when nuclei are clustered. Although many deep learning-based methods Akram *et al.* (2016); Naylor *et al.* (2019); Sornapudi *et al.* (2018); Sirinukunwattana *et al.* (2016); Cui *et al.* (2018); Fehri *et al.* (2019); Saha *et al.* (2018); Hollandi *et al.* (2019); Mahmood *et al.* (2018) performed very well for nucleus segmentation, learning these models requires a large set of human annotated samples, which may add to the time cost. In addition, a pre-trained deep learning model Akram *et al.* (2016) may not obtain satisfactory results on a new dataset, for example testing samples with severely clustered or overlapping nuclei (Fig. 1).

In this paper, we propose a constraint local thresholding (CLT) method for nucleus region detection and a marker controlled superpixel segmentation (MCS) method to automatically segment and count positive-stained nuclei on an IHC staining slide with a complex situation in order to compensate for the issues mentioned above. This is an improvement of our previous work Shu *et al.* (2013) which can produce more accurate nucleus segmentation and counting results. The first step is the detection of nucleus regions, using a fusing method to preserve nucleus intensity and shape characteristics that can compensate for the defects that arise by using only the intensity feature Shu *et al.* (2013) or shape feature Al-Kofahi *et al.* (2010). The second step is nucleus segmentation, which involves a two-tiered scheme to split severely overlapping or clustered nuclei. To improve the segmentation accuracy, we modified the scheme from seeds-based watershed segmentation Shu *et al.* (2013) to superpixel segmentation based on superseeds. The first tier is superseed detection, which forms a superseed centred at an initially detected seed point to involve both spatial and intensity features. The second tier is a modified efficient single pass superpixel segmentation which was applied to segment nuclei, depending on the results obtained by the previous tier. Finally, positive staining colour

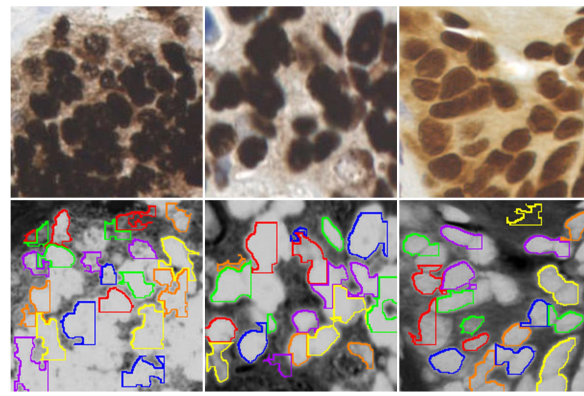


Fig. 1. Sample images with different issues, such as size and shape variation, intensity variation and severely clustering and overlapping. The first row is a set of three original sample images, images in the second row are the segmentation results generated by a published neural network-based nucleus segmentation model Akram *et al.* (2016).

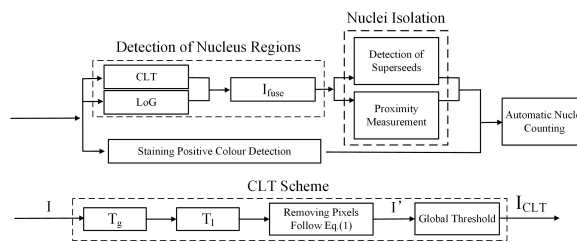


Fig. 2. Flowchart of nucleus counting method and CLT scheme.

pixels were detected by a statistical colour detection model Shu *et al.* (2016) and positive-stained nuclei were counted. We show that this MCS method can outperform existing methods for the segmentation and counting of nuclei in IHC stained slides with the issues mentioned above.

The rest of this paper is organised as follows: section 2 presents the framework of our proposed methods, section 3 shows the experimental results, and the conclusions are given in section 4.

2 Methods

In this paper, we propose a new nucleus segmentation and counting method to segment and count positive-stained nuclei in IHC stained slides with the issues mentioned above. Nuclei in such slides have large variations in size, shape and staining intensity, and severely clustered or overlapping nuclei are common. The workflow of the proposed method can be seen in Fig. 2.

2.1 Detection of nucleus regions

2.1.1 A fusing method

The detection of nucleus regions plays a key role in almost all nucleus segmentation methods. To cover uneven staining issues, we considered a new fusing method to combine intensity and shape characteristics to extract nucleus regions.

For intensity thresholding, we developed a constrained local thresholding method (CLT) scheme to extract nucleus pixels (Fig 2). This CLT scheme is different from the scheme introduced in Shu *et al.* (2013). Instead of sliding a local patch in a fixed step-size on all roughly detected nuclei pixels, we constrained the sliding of a local patch on the roughly detected nucleus boundary pixels. This modification can avoid determining the step-size and ensure computation efficiency. The first process of CLT

was to remove pixels that may be falsely identified as nucleus regions by global thresholding. These falsely identified nucleus pixels that are normally adjacent to nucleus boundaries. When nuclei are clustering or overlapping that may result in under-segmenting of clustered or overlapped nuclei. Thus, we intended to filter out these pixels by performing local thresholding in a limited region centred at the boundary of nucleus regions.

The original colour image was converted to a grayscale image I , followed by Gaussian smoothing with $radius = 2$. Two threshold values T_g , a global threshold, and T_l , a local threshold, were computed. The global threshold T_g was computed on the entire grayscaled image I to find the rough boundary of the nuclei. The local threshold T_l was computed from a local patch centred at each roughly detected nucleus boundary pixel after global thresholding using T_g . Pixels were identified as background and removed according to Eq.1.

$$f(p) = \begin{cases} I(p) & T_l < I(p) < T_g \\ 255 & \text{otherwise} \end{cases} \quad (1)$$

where p is the generic pixel in a local patch, $I(p)$ is the grayscale value of pixel p . Sliding this patch across the entire image and following Eq.1 can record all background pixels (marked with grayscale value 255 in image I') adjacent to the nuclei boundaries. Removing these pixels has the potential to help the auto-thresholding method to extract nucleus pixels and preserve nucleus contour characteristics. Then, a global threshold was applied to an image I' that was processed by the former scheme. Pixels in image I' whose grayscale value lower than this global threshold were considered to be nuclei pixels, and shown as black in I_{CLT} (Fig.3).

For the factor of shape, the blob-shape detecting method Laplacian of Gaussian (LoG), which has high computation efficiency, was considered Prodanov (2017). We used this method to highlight pixels with lower intensity values as nucleus pixels. After filtering across the entire image with LoG, pixels with a grayscale value of zero were set as nuclei pixels and a binary image I_{LoG} was obtained.

The CLT process can preserve nucleus edge pixels at the cost of missing nucleus pixels with brighter values. The LoG method can preserve most nucleus pixels at the cost of missing edge characteristics. In order to compensate for the defects arising in either method, a fusion method is a possible solution. Binary images obtained by these two methods are fused by using an OR operation, and object pixels in both images are combined together as final object pixels. The fused results are saved in a binary image I_{fuse} that circumvents the defects of either method in detecting nucleus regions (Fig.3).

2.1.2 The auto-thresholding method

The three thresholds used in the CLT scheme were obtained by the auto-thresholding method of Isodata Ridler and Calvard (1978) as follows.

$$M(t_i) = \frac{M_L(t_i) + M_H(t_i)}{2}, t_i \in [1, 254] \quad (2)$$

where t_i is a fixed point of the function $M(t_i)$, here t_i is the grayscale value from 1 to 254, $M_L(t_i)$ is the mean of all pixels in the image with a grayscale value less than or equal to t_i , $M_H(t_i)$ is the mean of all pixels in the image with a grayscale value greater than t_i . If $t_i = M(t_i)$ is satisfied, t_i is the obtained threshold T .

2.2 Nuclei isolation

Most of the positive-stained nuclei in IHC staining images are partially overlapping or clustered, which makes them difficult to count. The extracted nucleus regions must be split into isolated nuclei before counting. It has been demonstrated that using intensity, size and shape characteristics

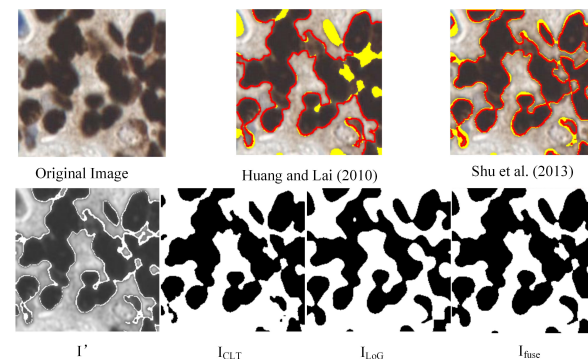


Fig. 3. Results of nucleus regions detection methods. The top row is the result of Huang and Lai (2010) and Shu *et al.* (2013) and the bottom row is the result of the proposed fusing method. Red pixels are the contour of detected nucleus regions by Huang and Lai (2010) and Shu *et al.* (2013). Yellow pixels are differences compared to I_{fuse} .

might achieve this purpose Shu *et al.* (2013). Rather than considering these characteristics separately as in the previous study, we aimed to develop a systematic method to trade-off these three characteristics.

Superpixel segmentation Ren and Malik (2003) is such a method as it systematically combines spatial and intensity characteristics in segmentation. A simple linear iterative clustering algorithm (SLIC) Achanta and Shaji (2012) has been demonstrated to segment objects into a number of cells and accurately find the contours at a very fast speed. To segment nuclei, we modified the superpixel segmentation algorithm proposed in Achanta and Shaji (2012) by adding a set of constraints to isolate clustered or overlapping nuclei. For initial seed points placement, in SLIC, they sampled pixels on a regular grid spaced S pixels apart. Here we defined the initial seed clusters, superseeds, obtained through the shape-based watershed. For the distance between a pixel and a cluster centre, we used a feature map I_m and the searching iterations d_s to compute a novel distance measure.

The proposed marker controlled superpixel segmentation is a two-tiered scheme and includes superseed detection and proximity measuring (Alg. 1, Alg. 2 and Fig. 4(a)).

Algorithm 1 The first tier of nucleus segmentation scheme.

Require: Binary image I_{fuse}
 Compute UEP-based watershed and remove noise particles
 Obtain centres of particles s_i
 Dilate s_i to S_i using β iterations on the mask image I_{fuse}
 Compute average intensity value Avg_i of S_i

2.2.1 Pre-processing

In preprocessing, several mask images such as I_m , I_p and I_b are pre-computed.

The mask image I_m preserves the results obtained by a dual-morphological transform scheme Huang and Lai (2010); Veta *et al.* (2011), i.e. open-by-reconstruction followed by close-by-reconstruction. Transformation processes are based on a predefined structural disk similar to basic open and close. This combination process has been demonstrated to preserve the shape of nuclei and to remove most of the noise that has a smaller size than the radius of this disk. Pixels with intensity variations are reduced and the differences between objects and background are increased. The morphological transform scheme results in constraining

Algorithm 2 The second tier of nucleus segmentation scheme.

Require: $S_i[Avg_i \gamma x_i y_i]$

Mask I_m , the dual-morphological transformation of I
 Mask I_p , a colour image with detected positive staining colour pixels
 Mask I_b , a binary image, binarize image I_m with a global threshold
 Set values for parameter θ and γ and set $iter = \beta$
repeat
 Increase $iter$ by one
 for Each $S_i[Avg_i \gamma x_i y_i]$ based on I_b **do**
 if Searching pixels are recorded by $S_j, j \neq i$ **then**
 Record pixels as splitting line pixels
 else
 for Searching each unrecorded pixel close to S_i **do**
 Set $Count_i = 0$
 Compute $Proxi$ based on I_m and $iter$
 if $Proxi > \theta$ **then**
 Record pixels as background pixels
 else
 Record pixels as nucleus pixels of S_i
 end if
 end for
 Set $Count_i$ to the number of searched unrecorded pixels
 if $Count_i \leq \gamma$ **then**
 Set S_i as unrepeatable
 end if
 end if
 end for
until All S_i are unrepeatable
 Remove pixels set as background and splitting line
 Remove noisy particles and remove noisy pixels through open processing
 Determine positive-stained nuclei according to I_p

intensity variations, which is beneficial to determining the weight value of superpixel segmentation.

Then, a global threshold (obtained by Isodata Ridler and Calvard (1978)) was applied to an image I_m . Pixels in image I_m whose grayscale value lower than this global threshold were set to black to get the binary image I_b . This mask image is used to limit the search pixels to potential nuclei pixels.

The mask image I_p preserves the positive-staining colour of pixels detected by a statistical colour detection model Shu *et al.* (2016). The model used in this paper is a pre-trained model embedded in their plugin. Pixels saved in image I_p with original colours are used to determine whether the segmented objects are stained positively or not.

2.2.2 Detection of superseeds

The first tier obtains initial seeds of nuclei and produces superseeds. This paper considered the shape-based watershed method described in Shu *et al.* (2013) to obtain the initial seeds. Shape-based watershed segmentation only depends on the shape characteristics of nuclei and is suitable to compensate for issues of both intensity variations and intensity with constant values (Alg. 1).

The shape-oriented method of Ultimate Eroded Points (UEP) based watershed Shu *et al.* (2013) was applied to the binary image I_{fuse} with detected nucleus regions. The main purpose of this tier is to isolate or split the clustering or overlapping nuclei into several nucleus-like particles. Although this is not an accurate isolation and some splitting lines are falsely located, it is beneficial to obtain initial seeds. Noise particles with small sizes are removed by a size filtering process. The centres of preserved particles are recognised to be initial seed markers s_i and dilated ones to

be superseeds S_i with β iterations (one pixel in radius). This dilation is limited by the mask image I_{fuse} . Then, the average intensity value Avg_i of all pixels belonging to the superseed S_i was computed based on I_m . Instead of measuring colour proximity in SLIC, we measured the grayscale intensity proximity for segmenting nuclei. Thus, the following proximity measurement procedure begins with centres $S_i = [I_i \ x_i \ y_i]$. According to the computed average intensity value of each superseed and a proposed local constraint γ , beginning centres can be modified to $S_i = [Avg_i \ \gamma \ x_i \ y_i]$.

2.2.3 Proximity measurement

The second tier is a proximity measurement process that systematically combines intensity, size and shape characteristics in segmentation. This tier is proposed with two purposes, i.e. to segment each nucleus and to re-adjust splitting lines (Alg. 2).

This proximity measurement process is a single pass clustering process. SLIC is implemented with multiple iterations to re-locate centres at the correct locations. The proposed MCS method centres at superseeds, detected by the first tier, and are fixed through the whole clustering process. For this single pass clustering processing, intensity proximity measuring and a spatial proximity measuring are processed as well. The process of producing a nucleus is similar to producing a superpixel cell in SLIC. This can be presented in computing proximity value between a pixel and cluster centre S_i as follows

$$Proxi = \sqrt{d_i^2 + (\frac{d_s}{\sigma})^2 \times \omega^2} \quad (3)$$

where d_i is the value of intensity distance, d_s is the value of spatial distance and ω is a fixed weight value and the maximum spatial distance σ . Computation based on Eq. 3 is a simplified measuring computation stated in Achanta and Shaji (2012) used in practice. ω is used to weigh the relatively importance between intensity proximity and spatial proximity. In nucleus segmentation, when ω is large, spatial proximity is more important and the resulting superpixels are more regular in size and shape. When ω is small, intensity proximity is more important and the resulting superpixels are more tightly adhered to edge-like pixels. Since falsely formed edges may spread everywhere due to uneven staining, it is better to measure pixels in pre-computed mask image I_m instead of the original image. By applying superpixel segmentation on mask image I_m , ω should be a large value, because spatial proximity is more important than intensity proximity.

Two features, intensity and spatial distance, are weighed to compute a spatial distance in a 2D feature space between searching pixels and a superseed. While this computation is processed on a dual-morphological processed image I_m , intensity differences across nuclei with clustering or overlapping are largely reduced. Thus, we transferred the spatial distance from 2D space to 1D space to simplify the proximity value computation in practice as:

$$Proxi = |d_i| + \frac{d_s}{\sigma} \times \omega \quad (4)$$

where $d_i = Abs(I_m(p) - Avg_i)$ is the absolute value of intensity distance between a searching pixel p (in the 3×3 neighborhood) and average intensity value of a superseed, d_s is the number of searching iterations, ω is a fixed weight value as well, and the maximum spatial distance σ is half of the mean size of normal nuclei.

The searching process performs like an iterative dilation of S_i with radius one on the mask image I_b . Dilated pixels with a computed proximity value less than a threshold θ are successfully clustered to S_i and referred to potential nuclei pixels. Conversely, dilated pixels are referred to as potential background. A splitting line is located at a dilated pixel that was clustered to another superseed in previous iterations.

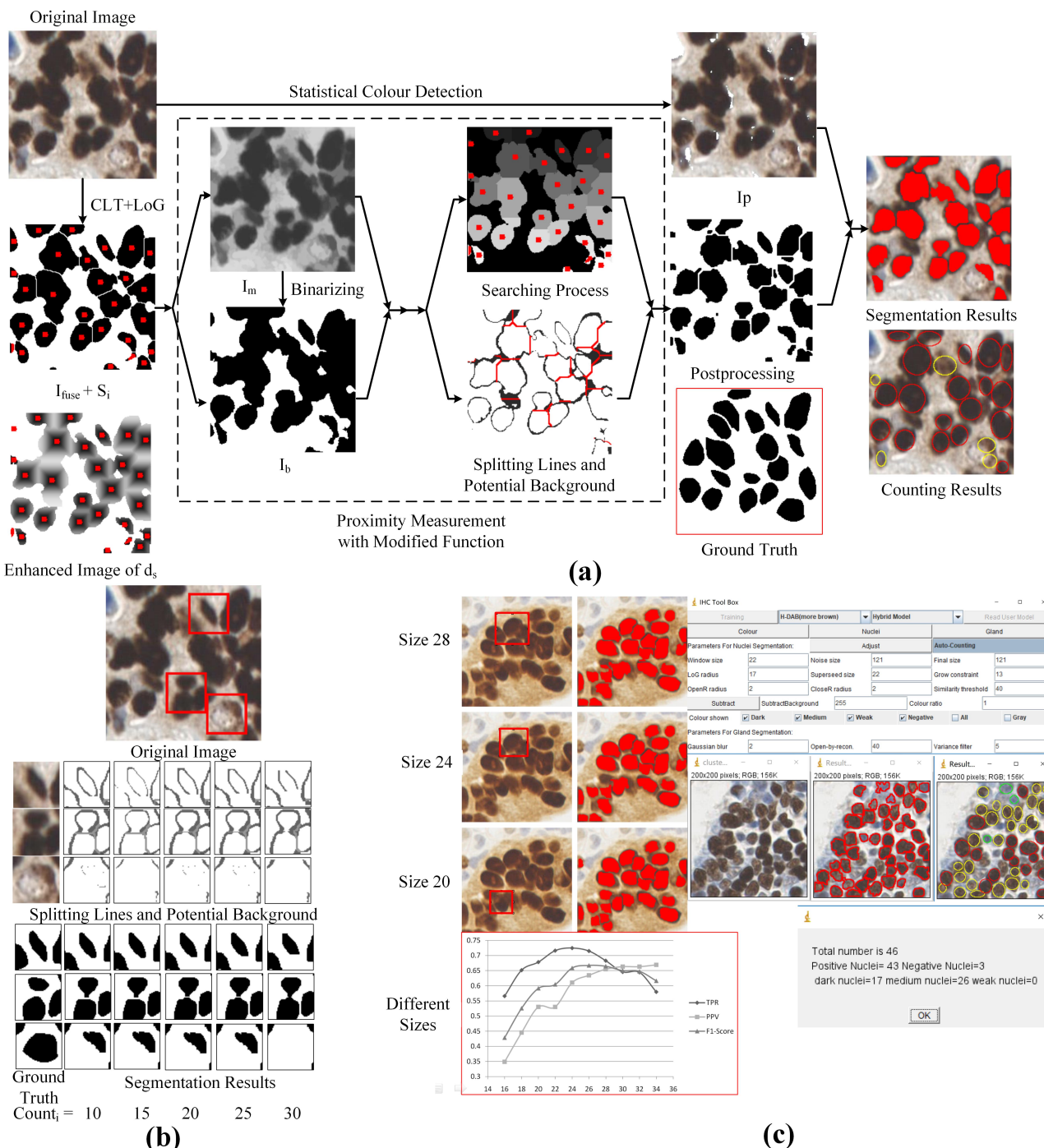


Fig. 4. Proposed method and the developed tool in ImageJ. (a) Two tier nucleus isolation process; (b) results obtained by a set $Count_i$ range from 10 to 30; (c) the developed tool in ImageJ.

Initially, the value of d_s equals β and $Count_i$ equals zero. For each iteration, d_s increases by one, while checking if the searching pixels are recorded. The $Count_i$ parameter counts the number of unrecorded pixels searched in one iteration. If the condition that $Count_i \leq \gamma$ is satisfied, the clustering process of a superseed S_i is stopped. This clustering process is repeated until all superseeds are stopped.

A higher value of $Count_i$ stops searching earlier, while a lower value of $Count_i$ stops searching later. An earlier stop to searching may result in

particles being removed as noise particles, because the sizes of segmented particles are smaller than their true sizes. A later stop to searching may result in obtaining the full sizes of isolated particles, but splitting lines may be located close to particles of a larger size in clustering or overlapping regions; see the locations of splitting lines in Fig. 4(b).

For postprocessing, pixels set as the splitting line and potential background are removed as background. Then, a morphological transform *open* was applied. Noise particles were removed after a size filtering

process and preserved particles were segmented nuclei. Finally, segmented nuclei that contained positively stained pixels in more than 10 percent of their segmented size were regarded as positively stained nuclei.

2.2.4 Automatic nucleus counting

Counting of positively stained nuclei was implemented by counting the segmented positively stained nuclei. The contour evidence of segmented nuclei was fitted with elliptical circles. Ellipse fitting has the benefits of maximally capturing nucleus information for further studies Phouladhy *et al.* (2016). Focusing on nucleus counting, we developed a simple scheme to colour in these fitted ellipse circles depending on the shades of positively stained colour pixels.

This automatic counting scheme is based on two results, i.e. segmented positively stained nuclei and detected positively stained colour. For a segmented nucleus, each pixel inside is examined for its value and assigned to a staining group. Groups include a dark staining group in red, a medium staining group in yellow and a weak staining group in blue, according to the stain grouping conditions mentioned in Liu *et al.* (2018). A nucleus is coloured *Red*, if the number of pixels assigned to the dark staining group is larger than the number of pixels assigned to other staining groups. In addition, the number of pixels determined to be stained dark should be greater than 10 percent segmented nucleus size to designate this nucleus as a positively stained nucleus.

3 Experiments and Results

3.1 Datasets

Two datasets used in this paper are H-DAB stained TMA slides stained for the biomarker p53. These slides came from different specimens from different diseases and were scanned by a Hamamatsu scanner. Samples in the datasets were randomly captured from 23 TMA whole scanned slides, each slide has about 100 cores and prepared at 40 \times magnification. They were captured from different cores and have issues of uneven staining and severely clustering or overlapping nuclei. One dataset, DataSeg, was used for the nucleus segmenting evaluation; it contains 52 images with a dimension of 200 \times 200. Another dataset contains 88 images with a dimension of 1280 \times 1024 was used for the nucleus counting evaluation; it was separated into two sub-datasets, DataCount1 contains 33 images and DataCount2 contains 50 images. The images used for the nucleus counting evaluation tried to cover as many different situations of these cores as possible, while the fuzzy cores were ignored. They were captured at either a core centre or the centre of a region with a number of positively stained nuclei. Only a few images in either DataSeg or datasets used for the nucleus counting evaluation were captured from the same core. Both datasets were captured by NDP.view at 20 \times magnification from original colour images. In DataSeg, the number of manually labelled nuclei was 1,265, in which the delineated contour of each nucleus was verified by a pathologist. In DataCount1, two pathologists manually annotated 12,477 and 11,175 dots on positively stained nuclei. In DataCount2, another two pathologists manually annotated 18,854 and 17,005 dots on positively stained nuclei. Annotations were done by four pathologists marking dots on positively stained nuclei through the cell counter plugin in ImageJ. Datasets can be downloaded from a link shown in Supplementary information.

We also tested our method on a competition dataset, 2018 Data Science Bowl (DSB) competition, and we tested our method on a released dataset stage 1 test (DSB1). DSB1 included 65 images, which were acquired under a variety of conditions and vary in terms of cell type, magnification and imaging modality (brightfield vs. fluorescence). All images in DSB1 were inverted, converted to grey scale and enhanced by histogram equalisation before testing. The background of these images

Table 1. The evaluation of segmentation results of DataSeg.

Methods	MTPR	MPPV	MF1-Score	≥ 0.5	≥ 0.8
WBS Shu <i>et al.</i> (2013)	0.654	0.568	0.606	829	114
SS Borovec and Kybic (2014)	0.399	0.196	0.251	457	99
MLT Phouladhy <i>et al.</i> (2016)	0.115	0.352	0.168	129	57
FRS+C Zafari <i>et al.</i> (2015)	0.322	0.353	0.334	364	77
FRS+B Zafari <i>et al.</i> (2015)	0.401	0.447	0.420	454	127
AUTOstyle Hollandi <i>et al.</i> (2019)	0.497	0.562	0.514	608	272
First Tier	0.620	0.558	0.577	769	199
Proposed+S	0.673	0.574	0.615	848	209
MCS16	0.566	0.349	0.429	771	74
MCS18	0.651	0.446	0.526	854	149
MCS20	0.678	0.530	0.592	921	193
MCS22	0.716	0.530	0.605	921	193
MCS24	0.725	0.611	0.659	917	257
MCS26	0.715	0.635	0.668	917	257
MCS28	0.683	0.655	0.665	864	268
MCS30	0.646	0.663	0.650	813	270
MCS32	0.644	0.663	0.648	813	270
MCS34	0.580	0.670	0.617	716	251

is shown as white and nuclei are shown with intensity values lower than background (Fig. 5(a)). Dataset of DSB can be downloaded from <https://www.ncbi.nlm.nih.gov/pubmed/31636459>.

3.2 Evaluation methods

Segmentation and nucleus counting evaluations were only processed on positively stained nuclei; negatively stained nuclei were not considered. The evaluation of segmentation was based on the computed IOU (Intersection-over-Union) between segmented nuclei and annotated nuclei Hollandi *et al.* (2019). The segmentation results of DataSeg were evaluated by calculating the true positive rate (TPR) and the positive predictive value (PPV) Zafari *et al.* (2015), F1-Score, and the number of segmented nuclei with IoU values ≥ 0.5 or ≥ 0.8 . The segmentation results of DSB1 were evaluated by calculating the mean precision at different IoU thresholds, ranging from 0.5 to 0.95 with steps of 0.05 (DSB score).

An evaluation of the nucleus counting results was performed by calculating the Pearson correlation coefficient (PCC) (R square) between automatically generated nucleus counting results and the number of manually annotated markers.

3.3 Parameter configuration

The parameters in this method can be summarised into two aspects, including parameters for nucleus detection and parameters for nucleus isolation. In nucleus detection, parameters depend on the average size of large nuclei with a radius around 24 pixels. The radius of the CLT sliding window was 24 and the radius of LoG processing was 20. For nucleus isolation, partial parameters were determined according to intra-intensity variation. In the first tier of isolation, superseeds were set with a size limitation of 20 pixels and β was 5. For watershed, the seeds were obtained by UEP. In the second tier, the radius of the morphological process was 2 pixels, the fixed weight value ω was 40, the threshold value θ was 40 and the searching constraint *Count* was 15. To filter out noise particles, the minimum size of accepted particles was 150.

3.4 Experimental results and comparisons

Segmentation performance was evaluated by comparing our methods (MCS) with five existing methods, such as watershed-based nucleus

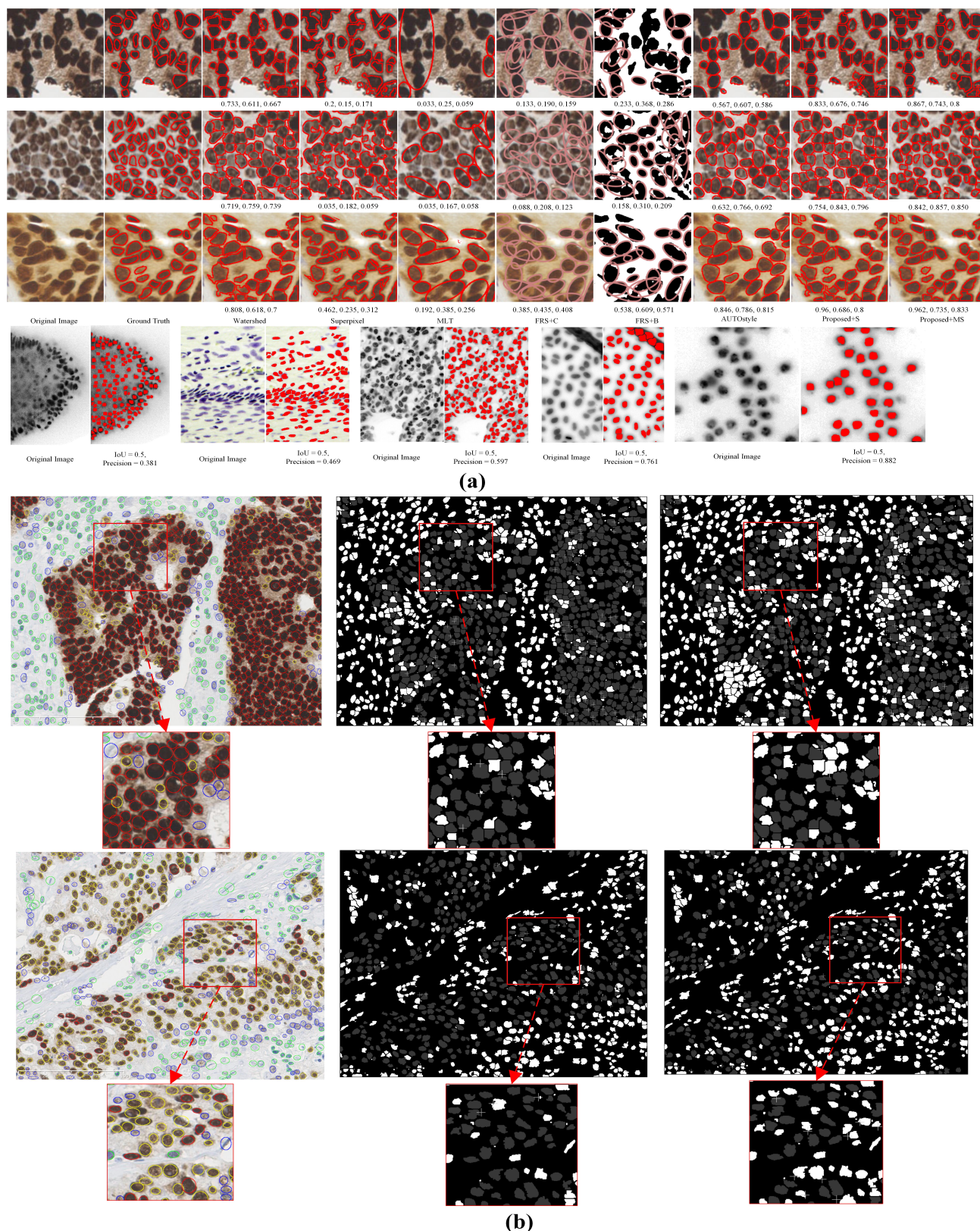


Fig. 5. Experimental results. (a) Several segmentation results of DataSeg and DSB1. For DataSeg, segmented results are shown in the top three rows with values of TPR, PPV and F1-Score; For DSB1, segmented results are shown in the bottom row with IoU and Precision. (b) Segmentation results of two samples from dataset used for the nucleus counting evaluation; the left column is the counting results on the original colour image with fitted colour ellipses; while the middle and right column are segmentation performance by comparing with pathologist one and two annotated markers. Particles filled with grey are correctly segmented nuclei; particles filled with white are false positive segmented nuclei or nuclei with negative staining colour; grey crosses are false negative segmented nuclei.

Table 2. The evaluation of segmentation results of DSB1.

Methods	DSB scores
GVF	0.205
CellProfiler	0.274
ilastik	0.319
unet4nuclei	0.065
AUTostyle Hollandi <i>et al.</i> (2019)	0.562
MCS	0.331 ± 0.006

segmentation (WBS) Shu *et al.* (2013), superpixel segmentation (SS) Borovec and Kybic (2014), the multi-level thresholding method (MLT) Phouлади *et al.* (2016), fast radial symmetry nucleus segmentation (FRS) Zafari *et al.* (2015) and the winner of the 2018 DSB competition, AUTostyle Hollandi *et al.* (2019). We also compared the proposed nucleus isolation method with the original superpixel function (Proposed+S) as stated in Eq. 3 and the segmented results after the first tier process (First Tier). Positively stained colour pixels were detected using a published pre-trained statistical model, which achieved the best performance in Shu *et al.* (2016). Although we applied a pre-trained neural network model published in Akram *et al.* (2016) on both datasets, the generated segmentation results were hard to compare and we did not have enough manually labelled samples to re-calibrate a new model.

The IoU-based comparison results are shown in Table 1. The calculated results are the mean values of TPR, PPV and F1-Score of 52 images. The best results were obtained by our proposed MCS method with mean F1-score 0.668. The results obtained by the proposed method with the original superpixel function were a little bit better than the previous watershed-based method. The results generated by FRS with binarised nucleus regions were much better than the results generated by FRS with original colour images. Before evaluating the AUTostyle Hollandi *et al.* (2019) segmented results on DataSeg, we manually removed segmented nuclei with negative stained colour and false positive segmented nuclei with a small size. AUTostyle with the pre-trained model delineated nucleus contour much better than our proposed method, which achieved the highest number of 272 when IoU was larger than 0.8. However, this deep learning-based method still could not isolate severely clustered or overlapping nuclei (Fig. 5(a)).

We also show the IoU-based segmentation results of the proposed method tested on DSB1 in Table 2. The results of several methods presented by Hollandi *et al.* (2019) are stated here as well. By testing on DSB1, the developed MCS method-based tool calibrated its parameters for each image through an easy parameter calibration function developed in the tool. This is because the size of nuclei and magnifications have broad variations across samples, and this tool may not compensate for such a wide range change of size with a fixed set of parameters. Three users participated in this evaluation process. The result obtained by the tool with mean DSB score 0.331 ± 0.006 was higher than the other results, except the top score winner AUTostyle Hollandi *et al.* (2019).

Nucleus counting results were evaluated by comparing our methods (MCS) with existing methods that obtained high values in the previous segmentation evaluation. Images in DataCount1 and DataCount2 have much greater dimension and many more nuclei, which were annotated by a dot marker in each nucleus. The parameters used in this evaluation were the same as those used in the segmentation experiment. The results are shown in Fig. 6. The linear curves show that our proposed method tended to overestimate the number of nuclei, with about 69 counts more per image. This is slightly larger than 46 counts associated with interobserver variability. If one considers that the average number of nuclei per image is about 600, this

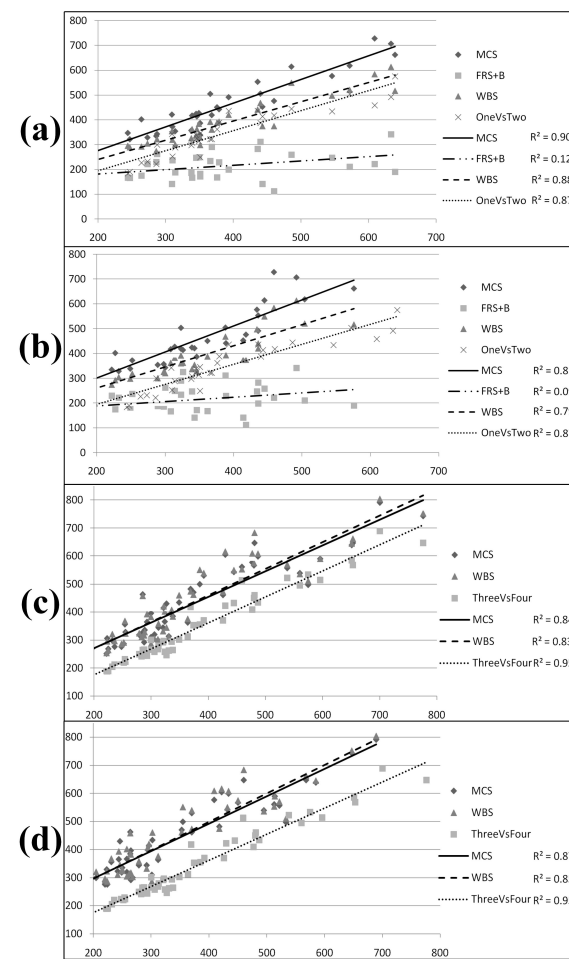


Fig. 6. Evaluation of counting results of DataCount1 and DataCount2. These are R square values between generated results and annotated nucleus counting results. The solid line is the proposed MSC, the dashed line is WBS, and the dashed/dotted line is FRS+B. (a)&(b) Results against pathologists one and two in DataCount1; (c)&(d) results against pathologists three and four in DataCount2.

may have little effect on the final outcome. Due to interobserver variability, the absolute nuclei counts may be less important than correlations between observers. We obtained high Pearson correlation coefficients of 0.949 ($R^2 = 0.901$, p-value <0.001) in DataCount1 and 0.934 ($R^2 = 0.871$, p-value <0.001) in DataCount2 between the generated results and the annotated nucleus counting results. The results on evaluating segmentation performance using the nucleus counting dataset are shown in the appendix and several segmentation samples are shown in Fig. 5(b).

3.5 A developed tool in ImageJ

We developed an MCS method-based tool in ImageJ with an easy parameter calibration function that can automatically calibrate its parameters through the box selection of any nucleus in an image. This simple function depends on the ratios between nucleus size and other parameters stated in Sec. 3.3. To segment a single nucleus, the size of the rectangular box should be larger than the selected nucleus, while for splitting clustered or overlapped nuclei, the rectangular box should be tight to the nucleus (Fig. 4(c)). By testing the calibration function, we selected a set of boxes with sizes ranging from 16 to 34 with steps of 2; the results are shown in Table 1 and Fig. 4(c). While selecting a box tight to a small nucleus, the number of segmented nuclei with IoU at 0.5 might be higher,

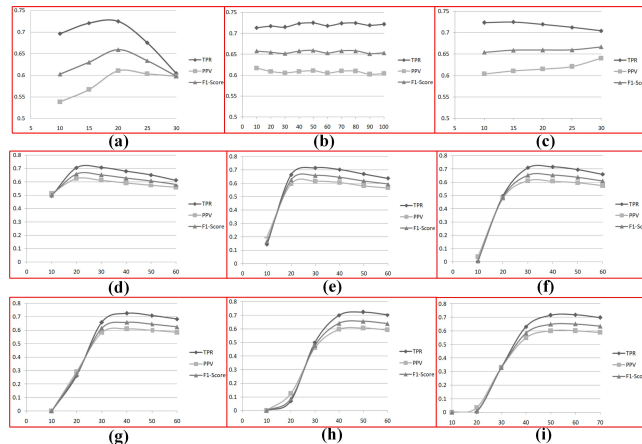


Fig. 7. Parameter tested results. (a) LoG tested results; (b) superseed size tested results; (c) Count tested results; (d-i) ω and θ tested results. The X axis is the parameter change range and the y axis is the experimental results.

but the other evaluation results might be lower, and by selecting a box larger than a normal nucleus, the evaluation results might be higher except for the number of segmented nuclei with IoU at 0.5.

Compared with deep learning methods, our developed MCS method-based tool may perform better in segmenting nuclei in DataSeg than that of Akram *et al.* (2016) and AUTOstyle Hollandi *et al.* (2019) and in DSB1 than that of unet4nuclei Hollandi *et al.* (2019). However, a well-trained deep learning model, i.e. a model trained with 100,000 annotated nuclei by AUTOstyle Hollandi *et al.* (2019) performed much better in segmenting nuclei in DSB1 than that of the tool. After training, the deep learning model segmented nuclei quickly, i.e. about 8 seconds per image either for DSB1 or DataSeg without postprocessing, but could not process images in DataCount either at the original size or resized to half of its original size. The mean computation time of our developed tool for DSB1 was 3.8 seconds, for DataSeg is 1 seconds and for DataCount 23.97 seconds. However, the time of annotating ten thousand nuclei may require 50 hours Caicedo *et al.* (2019). We only need a few seconds to calibrate parameters observed by an expert and the tool is flexible to use.

3.6 Parameter sensitivities evaluation

Different values of parameters were tested and compared in this section. For the morphological transformation, we tested single open-by-reconstruction and single close-by-reconstruction with the radius changing from 2 to 10. Open-by-reconstruction followed by close-by-reconstruction was also tested with the radius changing from 2 to 6. All these results were insensitive to radius changes, but the latter obtained better results than the other two. The searching constraint Count was tested and the results are shown in Fig. 7(c). With a larger searching constraint, a higher F1-score can be obtained. However, the cost of increasing the F1-score is a lower number of segmented nuclei and a lower number of correctly segmented nuclei.

For the modified superpixel function, we performed 36 tests by changing the weight value ω and the corresponding proximity threshold value θ . ω was changed from 10 to 50 and θ was changed from 10 to 70, (Fig. 7 (d) to (h)). When ω was set to 60, θ was changed from 20 to 70 (Fig. 7 (i)). These results show that this function does not work if θ is much lower than ω . To obtain the maximal results, the values of ω and θ should be the same or similar and can be determined according to the nucleus inner intensity difference.

4 Conclusion

This paper presents a new marker-controlled superpixel method for segmenting and counting nuclei in IHC stained images, brightfield images and fluorescent images. A CLT+LoG fusing method is proposed to extract nucleus pixels and preserve nucleus contour in nuclei clustering or overlapping regions. A two-tier scheme is proposed to isolate clustered or overlapped nuclei. We modified superpixel to be a segmentation method, instead of treating it as a tool in preprocessing. We compared this proposed method with several existing methods in both the segmentation and counting of nuclei in IHC stained images. The results show that our proposed method outperforms these existing nucleus segmentation methods and have very high correlations compared with the counting results of two pathologists. The proposed method was developed as a plugin in ImageJ and can be freely downloaded. By testing this tool on a competition dataset DSB1 that contains brightfield images and fluorescent images, the proposed method-based tool can also produce good results with little interobserver variation. This tool is easy to use and the parameters can be easily re-calibrated for segmenting cell-like objects in different kinds of images.

Acknowledgements

This work is partially supported by The National Natural Science Foundation of China(No.61371143) and Project No.1921 2019 The Fundamental Research Funds for Beijing Universities and 2019 Basic Scientific Research Project of Beijing Educational Committee-Nature Science Team Project and Industrial-University Cooperation and Collaborative Education Project for Higher Education Department of the Ministry of Education (No.201801121002) and Project of 2019 for Association of Computing Education in Chinese Universities(No.CERACU2019R05) and subject construction and cultivation of superiority subject program of the North China University of Technology (219051360018XN044).

References

- Al-Kofahi, Y. *et al* (2010) Improved automatic detection and segmentation of cell nuclei in histopathology images, *IEEE Transaction on Biomedical Engineering*, **57**(4), 841-852.
- Achanta, R. and Shaji, A. (2012) SLIC superpixels compared to state-of-the-art superpixel methods, *Pattern Analysis and Machine Intelligence*, **34**(11), 2274-2282.
- Akram, S.U. *et al* (2016) Cell segmentation proposal network for microscopy image analysis, *IEEE International Conference on Image Processing*, doi: 10.1109/ICIP.2016.7533216.
- Braun, M. *et al* (2013) Quantification of protein expression in cells and cellular subcompartments on immunohistochemical sections using a computer supported image analysis system, *Histol Histopatholo.*, **28**, 605-610.
- Borovec, J. and Kybic, J. (2014) jSLIC: Superpixels in ImageJ, *Computer Vision Winter Workshop*.
- Barricelli, B.R. *et al* (2019) ki67 Nuclei detection and ki67-index estimation: a novel automatic approach based on human vision modeling, *BMC Bioinformatics*, **20**, 733.
- Casiraghi, E. *et al* (2017) MIAQuant, a novel system for automatic segmentation, measurement, and localization comparison of different biomarkers from serialized histological slices. *European Journal of Histochemistry*, **61**(4):2838. doi: 10.4081/ejh.2017.2838.
- Casiraghi, E. *et al* (2018) A novel computational method for automatic segmentation, quantification and comparative analysis of

- immunohistochemically labeled tissue sections, *BMC BioInformatics*, **19(Suppl 10)** 357, doi: 10.1186/s12859-018-2302-3.
- Cui, Y. et al (2018) A Deep Learning Algorithm for One-step Contour Aware Nuclei Segmentation of Histopathological Images, arXiv:1803.02786.
- Caicedo, J.C. et al (2018) Evaluation of Deep Learning Strategies for Nucleus Segmentation in Fluorescence Images, *Cytometry Part A*,**8**:doi.10.1101/335216.
- Fehri, H. et al (2019) Bayesian polytrees with learned deep features for multi-class cell segmentation, *IEEE Transactions on Image Processing*, **28(7)**, 3246-3260.
- Huang, P.W. and Lai, Y.H. (2010) Effective segmentation and classification for HCC biopsy images. *Pattern Recognit.* **43(4)**: 1550-1563.
- Hollandi, R. et al (2019) A deep learning framework for nucleus segmentation using image style transfer, DOI: 10.1101/580605.
- Irshad, H. et al (2014) Methods for nuclei detection, segmentation, and classification in digital histopathology: A review-current status and future potential, *IEEE Rev Biomed Eng.*, **7**, 97-114.
- Liu, J. et al (2018) An End-to-End Deep Learning Histochemical Scoring System for Breast Cancer, *IEEE Transactions on Medical Imaging*, **99**.
- Mahmood, F. et al (2018) Deep adversarial training for multi-Organ nuclei segmentation in histopathology images, arXiv:1810.00236.
- Naylor, P. et al (2019) Segmentation of Nuclei in Histopathology Images by deep regression of the distance map, *IEEE Transactions on Medical Imaging*, **38(2)**, 448-459.
- Phoulady, H.A. et al (2016) Automatic quantification and classification of cervical cancer via adaptive nucleus shape modeling, *IEEE International Conference on Image Processing*, 2658-2662.
- Prodanov, D. (2017) Mexican Hat Filter, A Plugin of ImageJ.
- Ridler, T.W. and Calvard, S. (1978) Picture thresholding using an iterative selection method, *IEEE Transactions on Systems*, **8**, 630-632.
- Ren, X. and Malik, J. (2003) Learning a classification model for segmentation, in *Proc. IEEE Int. Conf. Comput Vis.*, 10-17.
- Shu, J. et al (2013) Segmenting overlapping cell nuclei in digital histopathology images, *35th IEEE Engineering in Medicine and Biology Society (EMBC)*, 5445-5448.
- Shu, J. et al (2016) Statistical colour models: an automated digital image analysis method for quantification of histological biomarkers, *BioMedical Engineering OnLine*, doi:10.1186/s12938-016-0161-6.
- Sirinukunwattana, K. et al (2016) Locality sensitive deep learning for detection and classification of nuclei in routine colon cancer histology images, *IEEE Transactions on Medical Imaging*, **35(5)**, 1196-1206.
- Saha, M. et al (2017) An advanced deep learning approach for Ki-67 stained hotspot detection and proliferation rate scoring for prognostic evaluation of breast cancer, *Scientific Reports*, **7**, Article number: 3213.
- Sornapudi, S. et al (2018) Deep Learning Nuclei Detection in Digitized Histology Images by Superpixels, *Journal of Pathology Informatics*, **9(1)**, 5.
- Veta, M. et al (2011) Marker-controlled watershed segmentation of nuclei in H&E stained breast cancer biopsy images, *In International Symposium on Biomedical Imaging (ISBI)*, 618-621.
- Wang, P. et al (2015) Automatic cell nuclei segmentation and classification of breast cancer histopathology images, *Signal Processing*, **122**, 1-13.
- Zafari, S. et al (2015) Segmentation of overlapping elliptical objects in silhouette images, *IEEE Transactions on image processing*, **24(12)**, 5942-5952.
- Zhang, W. and Li, H. (2017) Automated segmentation of overlapped nuclei using concave point detection and segment grouping, *Pattern Recognition*, **71**, 349-360.